

Intrinsic versus extrinsic cellular decision making

Louis González,¹ Bumsoo Han,^{2,3,4} and Andrew Mugler^{1,*}

¹*Department of Physics and Astronomy, University of Pittsburgh, Pittsburgh, PA 15260, USA*

²*Department of Mechanical Science and Engineering,
University of Illinois, Urbana-Champaign, Urbana, IL 61801, USA*

³*Cancer Center at Illinois, University of Illinois Urbana-Champaign, Urbana, IL 61801, USA*

⁴*Chan Zuckerberg Biohub Chicago, Chicago, IL 60642, USA*

A cell routinely responds to one of many competing environmental cues. Does the cell have an intrinsic preference for that cue, or does that cue have the highest extrinsic information content? We introduce a theoretical framework to answer this fundamental question. We derive extrinsic detection limits for four types of directional cues—external and self-generated chemical gradients, fluid flow, and contact inhibition of locomotion—and thus predict extrinsic decision boundaries when these cues compete as pairs. Comparing the boundaries to published data from cell migration experiments quantitatively determines the degree to which cell decisions are intrinsic vs. extrinsic, revealing the extent of cells’ autonomy and providing interpretation of their response networks.

Cells function in the presence of many competing environmental signals. These signals include chemical cues, mechanical cues, and cues from other cells. The traditional approach to understanding a cell’s response to an environmental cue focuses on characterizing the cell’s internal signaling network, which is ultimately responsible for transforming the cue into an observable behavior [1–3]. A markedly different approach focuses on the information contained in the cue itself, investigating whether a cell’s response approaches that of an optimal physical detector [4–9]. It is not clear which approach to use to understand a cell’s response to two or more competing cues: does the cell respond to the cue best matched to its intrinsic signaling network, or does it respond to the cue with the most extrinsic information? Here we make this fundamental question quantitative.

We focus on the ubiquitous response of cell migration. Migration is a cornerstone of tissue development [10], wound healing [11], and disease progression [12], notably in cancer [13]. Migration is guided by directional cues. Metastatic cancer cells, for instance, respond to chemical gradients [14–16], including self-generated gradients [17], as well as other directional cues such as pressure gradients generated by fluid flow [18, 19]. Migratory cells also respond to each other’s presence through a process known as contact inhibition of locomotion, where cell-cell contact results in migration reversal [20, 21]. These cues often occur simultaneously, such as in complex tissue environments or tumors. This makes the question of responding to competing directional cues both fundamentally interesting and physiologically relevant.

Here we investigate three experimentally motivated scenarios in which cells must respond to one of two competing cues (Fig. 1): (a) an autologous (self-generated) chemical gradient vs. a flow-induced pressure gradient, (b) an exogenous chemical gradient vs. a flow-induced pressure gradient, and (c) an exogenous chemical gradient vs. contact inhibition of locomotion from another cell. We first focus on the extrinsic information contained

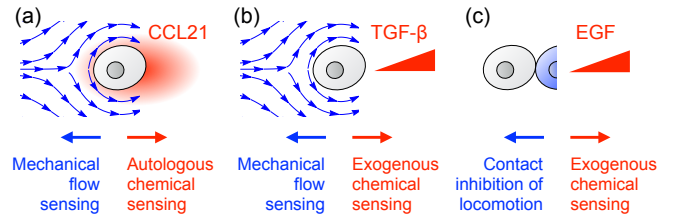


FIG. 1. The three experimentally motivated examples we investigate, where competing cues promote opposite migratory outcomes for a cell.

in each signal, deriving physical bounds on the precision with which each could be sensed. This approach leads to extrinsic decision boundaries separating phases where the cell is predicted to follow one cue over the other. Because each scenario corresponds to published experiments in which all free parameters have been measured, our theory makes falsifiable predictions that the published data either do or do not obey. Interestingly, we find that the extrinsic decision boundary is obeyed in case (a), partially obeyed in case (b), and violated in case (c). Therefore, we end by focusing on the implications of these findings for the intrinsic signaling network in each case. Throughout, our theory is built on simple scaling arguments because, when decision boundaries are violated, they are violated by orders of magnitude. This allows us to elucidate the rich physics underlying each sensing mode.

Autologous chemical sensing vs. mechanical flow sensing. In the presence of a slow background fluid flow, multiple cancer cell types have been shown to secrete and detect a chemical called CCL21 whose distribution is biased by the flow [17, 22]. This creates a downstream gradient that cells track, a process termed autologous chemotaxis [17]. However, at high cell density, these cells instead migrate upstream due to mechanical sensing of the flow-induced pressure gradient across the cell body [18]. The hypothesis is that high cell density corresponds to a large

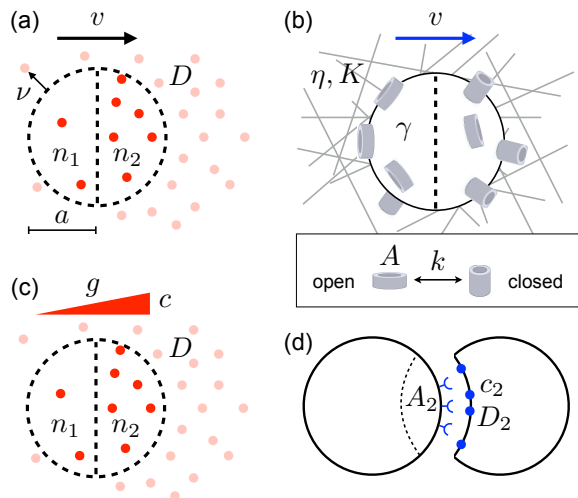


FIG. 2. Schematics of (a) autologous chemical sensing, (b) mechanical flow sensing, (c) exogenous chemical sensing, and (d) contact inhibition of locomotion. See text and Table I [25] for parameter descriptions.

background concentration of the secreted chemical, saturating the chemical gradient and allowing pressure sensing to take over [18, 23]. Thus far, this hypothesis has not been quantitatively tested.

We begin by deriving the physical limit to the precision of chemical gradient sensing for this process. Throughout this work we take precision to be the signal-to-noise ratio for a physical quantity that contains the directional information of the cue. For a chemical gradient, it suffices to consider the difference $\Delta n = n_1 - n_2$ in the number of molecules detected by the two halves of the cell [Fig. 2(a)] [7, 23, 24]. For slow flow, the mean of this difference scales as $\Delta \bar{n} \sim \epsilon \nu a^2 / D$ [23], where a is the cell length-scale, ν is the molecule secretion rate, D is the molecular diffusion coefficient, and the flow speed v enters through the Peclet number $\epsilon = \nu a / D \ll 1$ (see Table I in the Supplemental Material [25] for a list of all parameters in this work, as well as their experimentally measured values). This expression for $\Delta \bar{n}$ follows from taking, in each half of the cell, the ratio of the rates of molecule gain due to secretion, and of loss due to diffusion and flow [23].

The variance in Δn scales the same way as the variance in the total number n of molecules detected by the cell [7]. Because diffusion is Poissonian, this variance equals its mean \bar{n} . In a time τ , the variance can be reduced as $\sigma_{\Delta n}^2 \sim \bar{n} / M$ by the cell integrating $M = D\tau / a^2$ independent measurements, where M follows from dividing τ by the diffusive correlation time a^2 / D [4]. The mean scales as $\bar{n} \sim \nu a^2 / D + ca^3$, where the first term corresponds to molecules secreted by the cell, and the second term corresponds to a background concentration c of molecules secreted by other cells [23]. The background concentration is related to the cell density ρ by balancing molecule se-

cretion with molecule loss from flow, giving $c = (\nu L / v)\rho$, where L is the length of the experimental environment in the flow direction [23].

Putting these results together, we arrive at the precision of autologous chemical sensing,

$$\mathcal{P}_{\text{chem}}^{\text{auto}} = \frac{\Delta \bar{n}}{\sigma_{\Delta n}} \sim \epsilon \sqrt{\frac{\epsilon \nu \tau}{\epsilon + \rho a^2 L}}, \quad \text{with } \epsilon = \frac{\nu a}{D}. \quad (1)$$

This expression demonstrates that precision increases with faster flow, via ϵ , but decreases with higher cell density ρ . Although it is derived using simple scaling arguments, these scalings are validated by the fact that expressions for $\Delta \bar{n} / \sigma_{\Delta n}$ with $\rho = 0$, and for $\Delta \bar{n} / \bar{n}$ with $\rho > 0$, agree [26] with more rigorous results derived by us previously using a reaction diffusion treatment that accounts explicitly for the fluid flow field [8, 23].

We now seek to compare this result with the physical limit to the precision of mechanical sensing of the flow. Previous work derived this limit for cells detecting a flow via mechanosensitive ion channels that respond to changes in membrane tension when the flow induces a shear [6]. However, when cells are embedded in a dense extracellular matrix, as in the experiments [18, 19], the flow is low-permeability, meaning that the average pore size of the matrix is much smaller than the cell. At low permeability, the force on the cell due to the flow is dominated by pressure, not shear [19]. Therefore we adapt the previous treatment to pressure sensing. Again, we focus on simple scaling arguments, which to our knowledge are absent from the literature for this process.

The flow induces a pressure difference ΔP across the cell. At low permeability $K \ll a^2$, the pressure difference scales with the flow velocity v as $\Delta P \sim \eta \nu a / K$ [19], where η is the fluid viscosity. The pressure difference causes a membrane tension difference via the Young-Laplace equation, $\Delta \gamma \sim a \Delta P$. As in the previous work [6], we suppose that the cell detects this tension difference using N ion channels distributed across the membrane [Fig. 2(b)]. Each channel switches between an open and a closed conformation. The probability p that the channel is open obeys that for a two-state system in a thermal bath, $p = (1 + e^{-q})^{-1}$, where $q = \beta \Delta E$ is the energy difference ΔE between the closed and open states, scaled by the inverse temperature β . The energy difference is given by $\Delta E = \Delta \gamma \Delta A$, where ΔA is the difference in channel area between the closed and open state [6, 27]. Thus, an increase in pressure on the upstream side of the cell causes an increase in membrane tension, which increases the probability that a channel there is open.

Just as the directional information of the chemical cue was contained in the difference in the detected molecule numbers from the two halves of the cell, here the directional information of the mechanical cue is contained in the difference in the (dimensionless) tension readouts q from channels on the two halves of the cell. On the upstream half the $N/2$ channels will read out a tension

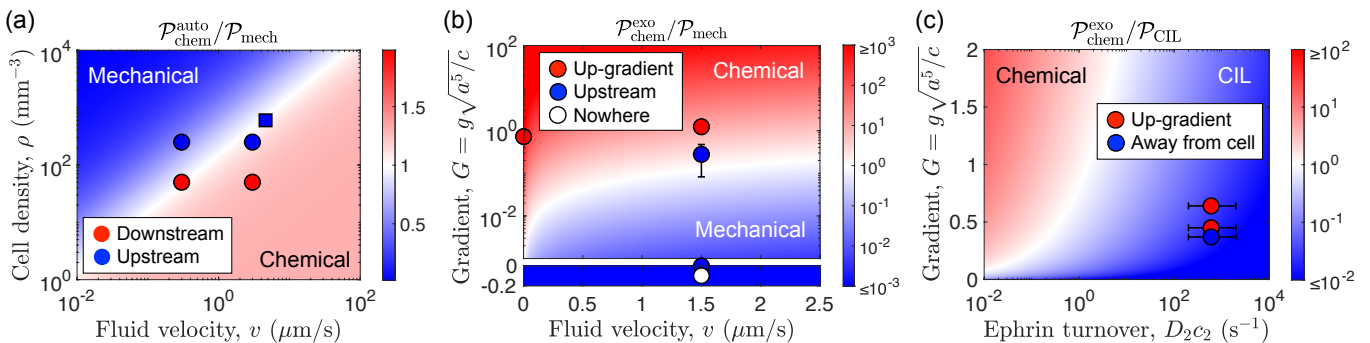


FIG. 3. Predicted extrinsic decision boundaries (color maps) and observed cell behavior (data points) for the three cases in Fig. 1. Data from [18] (a, circles), [19] (a, square), [16] (b), and [21] (c). See [25] for analysis details and [28] for code.

increase, whereas on the downstream half the $N/2$ channels will read out a tension decrease. Thus, the mean difference will scale as $\bar{Q} \sim (N/2)q - (N/2)(-q) = Nq$. The variance, assuming the channels are sufficiently independent [6], will scale as $\sigma_Q^2 \sim N\sigma_q^2/M$, where here $M = (k_+ + k_-)\tau$ because the correlation time is the inverse sum of the channel switching rates k_+ and k_- . The variance in q propagates in quadrature from $p = (1 + e^{-q})^{-1}$ as $\sigma_q^2 = 1/\sigma_p^2$, where $\sigma_p^2 = \bar{p}(1 - \bar{p})$ for a two-state switch. The minimum noise occurs when the channels have $\bar{p} = 1/2$ (and thus $k_+ = k_- \equiv k$) in the absence of flow, a condition called critical pre-stress [6].

Putting these results together, we arrive at the precision of mechanical flow sensing,

$$\mathcal{P}_{\text{mech}} = \frac{\bar{Q}}{\sigma_Q} \sim q\sqrt{Nk\tau}, \quad \text{with} \quad q = \frac{\beta\eta va^2 \Delta A}{K}. \quad (2)$$

This expression demonstrates that precision increases with faster flow, via q . Again, although it is derived using simple scaling arguments, it agrees with the previous work [6] in the case that tension change is induced by shear instead of pressure [29].

All parameters in Eqs. 1 and 2 have been measured experimentally (Table I [25]). Therefore, we can evaluate the ratio $\mathcal{P}_{\text{chem}}^{\text{auto}}/\mathcal{P}_{\text{mech}}$ with no free parameters. Figure 3(a) shows this ratio as a function of flow speed and cell density (color map). We see that, as hypothesized, the precision of mechanical sensing overtakes that of chemical sensing as the cell density increases. Overlaid as data points are the measured flow speeds and cell densities of cells that are observed to travel upstream or downstream [18, 19] (see [25] for details on how all data points in Fig. 3 are extracted). The data approximately agree with the decision boundary predicted by the precision ratio. This finding suggests that these cells decide between autologous chemical sensing and mechanical flow sensing based on extrinsic signal information.

Exogenous chemical sensing vs. mechanical flow sensing. We previously investigated a cancer cell line exposed to both a fluid flow and a gradient of an exoge-

nous chemical attractant TGF- β [16]. We found that in locations where the gradient was downstream and steep, cells migrated downstream. However, in locations where the gradient was downstream but shallow, cells migrated upstream. Here we ask whether these observations are consistent with the precision crossover between exogenous chemical sensing and mechanical flow sensing.

Our derivation for exogenous chemical sensing follows that above for autologous chemical sensing, but now the average number \bar{n} of detected molecules and the difference $\Delta\bar{n}$ between the two halves of the cell are set by the local background concentration c and gradient g of an exogenous chemical signal [Fig. 2(c)]. Specifically, we have $\bar{n} \sim ca^3$ and $\Delta\bar{n} \sim (ga)a^3$, where ga is the approximate concentration difference across the cell [7]. The other elements follow from above: $\sigma_{\Delta\bar{n}}^2 \sim \bar{n}/M$, with $M = D\tau/a^2$. Thus we arrive at the precision of exogenous chemical sensing,

$$\mathcal{P}_{\text{chem}}^{\text{exo}} = \frac{\Delta\bar{n}}{\sigma_{\Delta\bar{n}}} \sim G\sqrt{\frac{D\tau}{a^2}}, \quad \text{with} \quad G = g\sqrt{\frac{a^5}{c}}. \quad (3)$$

The dimensionless parameter G captures the fact that precision increases with the gradient but decreases with the background concentration: it is harder to measure a molecule number difference against larger background fluctuations [7]. Once again, although this expression is derived using simple scaling arguments, it agrees [30] with a more rigorous result derived by us previously using a reaction diffusion treatment that accounts for internal signaling within the detector [7].

Again, because all parameters in Eqs. 2 and 3 have been measured experimentally (Table I [25]), we can evaluate the ratio $\mathcal{P}_{\text{chem}}^{\text{exo}}/\mathcal{P}_{\text{mech}}$ with no free parameters. Figure 3(b) shows this ratio as a function of flow speed and dimensionless gradient strength G (color map). We see that chemical sensing is more precise for larger gradients, while mechanical sensing is more precise for larger flow speeds. Overlaid as data points are the measured flow speeds and G values from our previous experiments [16]. Most points agree with the decision boundary pre-

dicted by the precision ratio, with one point pushing the boundary but still within error. This suggests that in most cases the decision is based on extrinsic information. However, the notable exception is the white point deep within the blue regime: these cells are predicted to migrate upstream but are observed, on average, to migrate nowhere.

The difference between the white data point and the other data points in Fig. 3(b) is that the white point corresponds to a very high background concentration (see [25]). In fact, here the gradient even points slightly upstream ($g < 0$), meaning that, for this point only, both cues promote upstream migration with no conflict. Yet, the high background concentration evidently prevents cells from responding to either cue. This is in marked contrast to the previous case [Fig. 3(a)], where, like here, the high background concentration reduced the precision of chemical sensing below that of mechanical sensing, but unlike here, the cells indeed migrated upstream. This contrast has important implications for the intrinsic signaling networks in these two cases, which we expand upon in the Discussion.

Exogenous chemical sensing vs. contact inhibition of locomotion. Previous work investigated a cancer cell line exposed to a gradient of an exogenous chemical attractant EGF and placed in narrow channels [21]. This setup caused many encounters where up-gradient migration conflicted with repulsion from another cell due to contact inhibition of locomotion (CIL). At low background EGF concentration, cells migrated up-gradient, whereas at high background concentration, cells migrated away from the other cell. Here we ask whether these observations are consistent with the precision crossover between exogenous chemical sensing and CIL.

Recent work investigated the physical aspects of CIL accuracy [9] but focused on the effects of contact size and signal interference rather than a general precision limit. Here, as above, we derive the physical limit from simple scaling arguments. The mechanism of CIL is that each cell's membrane has molecules called ephrin, as well as receptors to detect that molecule on another cell [9, 21] [Fig. 2(d)]. Calling the contact area A_2 and the two-dimensional concentration of ephrin c_2 , the mean number of ephrin molecules scales as $\bar{n} \sim c_2 A_2$. Calling the diffusion coefficient of ephrin D_2 , the variance in this number, as above, scales as $\sigma_n^2 \sim \bar{n}/M$ with $M = D_2 \tau / A_2$. Thus we arrive at the precision of CIL,

$$\mathcal{P}_{\text{CIL}} = \frac{\bar{n}}{\sigma_n} \sim \sqrt{D_2 c_2 \tau}. \quad (4)$$

We note that the contact area A_2 drops out, which is consistent with the finding in the previous work that accuracy is largely insensitive to contact size [9].

Figure 3(c) shows the ratio $\mathcal{P}_{\text{chem}}^{\text{exo}} / \mathcal{P}_{\text{CIL}}$ as a function of ephrin turnover $D_2 c_2$ and dimensionless gradient strength G (color map), again with all remaining param-

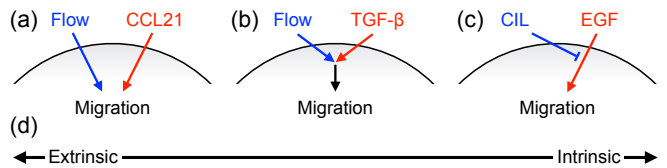


FIG. 4. Pathway structure (a) that we predict or (b, c) that is previously known from experiments. (d) The three cases define a spectrum from extrinsic to intrinsic decision-making.

eters measured experimentally (Table I [25]). We see that chemical sensing is more precise for larger gradients, while CIL is more precise for higher ephrin turnover. Overlaid as data points are the measured G values from the narrow channel experiments [21] and the values of $D_2 c_2$ from experiments that measured the diffusion and concentration of ephrin [31]. We see that the measured decision boundary is three orders of magnitude away from the predicted boundary. This finding suggests that these cells do not decide between exogenous chemical sensing and CIL based on extrinsic signal information alone. Specifically, it suggests that cells intrinsically weight information about the EGF gradient over information from CIL.

Discussion. What are the implications of Fig. 3 for the intrinsic signaling network in each case? The strong violation of the extrinsic decision boundary in Fig. 3(c) suggests that the EGF pathway and the CIL pathway interact upstream of the migration response, rather than transmitting the extrinsic information to the migration response independently. In fact, in the previous experimental work on this case [21], it was demonstrated that the ephrin receptor represses the activity of the EGF receptor directly, far upstream of the cascade that connects this activity to the migration response [Fig. 4(c)]. The cell could easily tune the strength of this repression, with weaker repression suppressing information from the CIL signal and shifting the decision boundary further into the naively CIL-dominated regime, as in Fig. 3(c).

Similarly, the violation of the extrinsic decision boundary at high background concentration in Fig. 3(b) (white point) but not Fig. 3(a) suggests that the TGF- β pathway and the flow sensing pathway converge upstream of the migration response. In fact, in our previous experimental work, we found that the results in Fig. 3(b), as well as many other results including cases of commensurate (rather than conflicting) cues, are explained by a model in which the two pathways transmit the extrinsic information to the migration response independently [Fig. 4(a)]. Taken together, our results imply a spectrum

of extrinsic to intrinsic decision-making for these three cases [Fig. 4(d)], with cases (a), (b), and (c) progressively more intrinsic, respectively.

By focusing on the physics of sensory precision, we have made quantitative and falsifiable the question of how cells respond to competing cues. Our approach can be extended straightforwardly to other cue types, to alternative cue pairings, and to competitions among more than two cues, or more than two responses. Our framework predicts the signals that cells transmit faithfully, and the signals that cells may suppress or ignore in favor of others. It facilitates the interpretation of signaling networks and may guide the discovery of pathways that are still poorly characterized.

We thank Hye-ran Moon and Andre Levchenko for helpful discussions. The code for Fig. 3 is freely available [28]. References [32–35] are in the Supplemental Material [25]. L. G. and A. M. were supported by National Science Foundation Grants No. PHY-2118561 and No. MCB-2118037. B. H. was supported by National Institutes of Health Grants No. R01 CA254110, No. R33 HL159948, and No. U01 CA274304.

* andrew.mugler@pitt.edu

- [1] L. H. Hartwell, J. J. Hopfield, S. Leibler, and A. W. Murray, *Nature* **402**, C47 (1999).
- [2] U. Alon, *An introduction to systems biology: design principles of biological circuits* (Chapman and Hall/CRC, 2019).
- [3] S. Saha, H.-r. Moon, B. Han, and A. Mugler, *npj Systems Biology and Applications* **8**, 48 (2022).
- [4] H. Berg and E. Purcell, *Biophysical Journal* **20**, 193 (1977).
- [5] R. G. Endres and N. S. Wingreen, *Proceedings of the National Academy of Sciences* **105**, 15749 (2008).
- [6] R. Bouffanais, J. Sun, and D. K. Yue, *Physical Review E - Statistical, Nonlinear, and Soft Matter Physics* **87** (2013), 10.1103/PhysRevE.87.052716.
- [7] A. Mugler, A. Levchenko, and I. Nemenman, *Proceedings of the National Academy of Sciences* **113**, E689 (2016).
- [8] S. Fancher, M. Vennettilli, N. Hilgert, and A. Mugler, *Physical Review Letters* **124**, 168101 (2020).
- [9] W. Wang and B. A. Camley, *Physical Review E* **109**, 054408 (2024).
- [10] A. J. Ewald, A. Brenot, M. Duong, B. S. Chan, and Z. Werb, *Developmental Cell* **14**, 570 (2008).
- [11] M. Phillipson and P. Kubes, *Nature Medicine* **17**, 1381 (2011).
- [12] B. A. Fenderson, *Shock* **24**, 402 (2005).
- [13] P. Friedl and K. Wolf, *Nature Reviews Cancer* **3**, 362 (2003).
- [14] B. J. Kim, P. Hannanta-Anan, M. Chau, Y. S. Kim, M. A. Swartz, and M. Wu, *PLoS one* **8**, e68422 (2013).
- [15] H.-r. Moon, S. Saha, A. Mugler, and B. Han, *Iscience* **24** (2021).
- [16] H. ran Moon, S. Saha, A. Mugler, and B. Han, *Lab on a Chip* **23**, 631 (2023).
- [17] J. D. Shields, M. E. Fleury, C. Yong, A. A. Tomei, G. J. Randolph, and M. A. Swartz, *Cancer Cell* **11**, 526 (2007).
- [18] W. J. Polacheck, J. L. Charest, and R. D. Kamm, *Proceedings of the National Academy of Sciences* **108**, 11115 (2011).
- [19] W. J. Polacheck, A. E. German, A. Mammoto, D. E. Ingber, and R. D. Kamm, *Proceedings of the National Academy of Sciences of the United States of America* **111**, 2447 (2014).
- [20] R. Mayor and C. Carmona-Fontaine, *Trends in cell biology* **20**, 319 (2010).
- [21] B. Lin, T. Yin, Y. I. Wu, T. Inoue, and A. Levchenko, *Nature communications* **6**, 6619 (2015).
- [22] J. M. Munson, R. V. Bellamkonda, and M. A. Swartz, *Cancer research* **73**, 1536 (2013).
- [23] M. Vennettilli, L. González, N. Hilgert, and A. Mugler, *Physical Review E* **106** (2022), 10.1103/PhysRevE.106.024413.
- [24] L. González and A. Mugler, *Physical Review E* **108** (2023), 10.1103/PhysRevE.108.054406.
- [25] See Supplemental Material for details on the analysis of previously published experimental data used in Fig. 3.
- [26] Specifically, $\Delta\bar{n}/\sigma_{\Delta n} = \epsilon\sqrt{\nu\tau}$ with $\rho = 0$ agrees with Eq. 15 in [8], and $\Delta\bar{n}/\bar{n} = \epsilon^2/(\epsilon + \rho a^2 L)$ agrees with Eq. 8 in [23], up to factors of order unity.
- [27] T. Ursell, J. Kondev, D. Reeves, P. A. Wiggins, and R. Phillips, *Mechanosensitive Ion Channels*, 37 (2008).
- [28] github.com/gonzalezlouis/decision-making.
- [29] Specifically, Eq. 2 agrees with Eqs. 41 and 42 in [6] up to factors of order unity when (i) the tension change $\Delta\gamma = a\eta G$ arises from the shear rate G rather than the pressure difference, (ii) critical pre-stress is assumed ($\Delta h - \gamma_0 \Delta A = 0$ there), and (iii) the membrane stretch energy (much smaller than the tension energy) is ignored. Note that k here then corresponds to $k_0 e^{-\beta\gamma_0 \Delta A/2}$ there, which given the parameter choices there evaluates to about once per second, consistent with the measured value we use here (Table I [25]).
- [30] Specifically, Eq. 3 agrees with Eq. 11 in [7] up to factors of order unity in the limit of a single cell ($n_0 = 1$ there).
- [31] Q. Xu, W.-C. Lin, R. S. Petit, and J. T. Groves, *Biophysical journal* **101**, 2731 (2011).
- [32] M. E. Fleury, K. C. Boardman, and M. A. Swartz, *Biophysical Journal* **91**, 113 (2006).
- [33] S. I. Sukharev, W. J. Sigurdson, C. Kung, and F. Sachs, *The Journal of general physiology* **113**, 525 (1999).
- [34] C. E. Morris, *The Journal of Membrane Biology* **113**, 93 (1990).
- [35] G. Shapovalov and H. A. Lester, *The Journal of general physiology* **124**, 151 (2004).

SUPPLEMENTAL MATERIAL

PARAMETER VALUES FOR THEORY

All parameters used for the theory color maps in Fig. 3 are listed in Table I. Their values are taken from published experimental studies, as follows:

- The experiments use MDA-MB-231 [18, 19], KIC [16], and MTLn3-B1 [21] cell lines, all of which have lengthscale on the order of $a = 10 \mu\text{m}$ (see microscopy images therein).
- MDA-MB-231 cells secrete CCL21 molecules (or the related CCL19 molecules, which bind to the same receptor) at a rate on the order of 1 s^{-1} (see Fig. 3F in [17] and the analysis in the third paragraph of [8]).
- The diffusion coefficient of CCL21 in extracellular matrix was estimated to be $D = 150 \mu\text{m}^2/\text{s}$ [32]. The molecular weights of TGF- β and EGF are similar to that of CCL21 (around 10 kDa), and therefore we use the same value of D .
- The chamber length in the flow direction for the autologous chemotaxis experiments was approximately $L = 3 \text{ mm}$ (see Fig. 1A in [18]).
- The permeability of 2 mg/mL type I collagen matrix was measured to be $K = 0.1 \mu\text{m}^2$ in [18]. The same density of type I collagen matrix was used in [16], and the permeability was estimated at a similar value of $K = 0.05 \mu\text{m}^2$.

a	Cell lengthscale	$10 \mu\text{m}$	[16, 18, 19, 21]
ν	Molecule secretion	1 s^{-1}	[17]
D	Molecule diffusion	$150 \mu\text{m}^2/\text{s}$	[32]
L	Chamber length	3 mm	[18]
K	Permeability	$0.1 \mu\text{m}^2$ $0.05 \mu\text{m}^2$	[18] Fig. 3(a) [16] Fig. 3(b)
ΔA	Channel area change	6.5 nm^2	[33]
N	Channels per cell	1000	[34]
k	Channel switching rate	1 s^{-1}	[35]
ρ	Cell density	Fig. 3(a)	[18, 19]
v	Fluid flow speed	Fig. 3(a, b)	[16, 18, 19]
c	Background conc.	Fig. 3(b, c)	[16, 21]
g	Concentration gradient	Fig. 3(b, c)	[16, 21]
c_2	Ephrin concentration	Fig. 3(c)	[31]
D_2	Ephrin diffusion	Fig. 3(c)	[31]
τ	Integration time	Drops out	
A_2	Cell-cell contact area	Drops out	
η	Viscosity	$10^{-3} \text{ Pa}\cdot\text{s}$	Water
β	Inverse temperature	$2.5 \times 10^{20} \text{ J}^{-1}$	Room temp.

TABLE I. Parameters used in this work.

- The conformational area change of mechanosensitive ion channel MscL was measured at $\Delta A = 6.5 \text{ nm}^2$ [33].
- Experiments find that mechanosensitive ion channels occur at a density on the order of $1 \mu\text{m}^{-2}$ that is notably uniform across the cell surface and ubiquitous across cell types (see [34] and references therein). Given a surface area of $4\pi a^2$ with $a = 10 \mu\text{m}$, we have on the order of $N = 1000$ channels.
- The residency times of mechanosensitive ion channels MscL and MscS were measured at approximately 1 s (see the top panels of Figs. 2 and 4A in [35]), giving a switching rate on the order of $k = 1 \text{ s}^{-1}$.

DATA POINTS

All data points plotted in Fig. 3 are taken from published experimental studies, as summarized in Table I. See [28] for the code and data.

Specifically, for Fig. 3(a):

- The cell seeding densities used in [18] are $\rho = 50 \text{ mm}^{-3}$ and $\rho = 250 \text{ mm}^{-3}$. The cell seeding density used in [19] is $\rho = 600 \text{ mm}^{-3}$.
- The flow speeds applied in [18] are $v = 0.3 \mu\text{m}/\text{s}$ and $v = 3 \mu\text{m}/\text{s}$. The flow speed applied in [19] is $v = 4.6 \mu\text{m}/\text{s}$.
- At $\rho = 50 \text{ mm}^{-3}$, cells migrated downstream on average for both flow speeds (see gray squares in Fig. 3B of [18]). At $\rho = 250 \text{ mm}^{-3}$, cells migrated upstream on average for both flow speeds (see gray circles in Fig. 3B of [18]). At $\rho = 600 \text{ mm}^{-3}$ and $v = 4.6 \mu\text{m}/\text{s}$, cells migrated upstream on average (see lower left plot in Fig. 5C of [19]).

For Fig. 3(b):

- The flow speed applied in [16] is $v = 1.5 \mu\text{m}/\text{s}$.
- The gradient g and average background concentration c are computed between all pairs of data points in [16] with (i) no flow (Fig. 2D in [16]), (ii) a large downstream gradient (right region of Fig. 2F in [16]), and (iii) a small upstream gradient (right region of Fig. 2E in [16]). The values of $G = g\sqrt{a^5}/c$ are calculated with $a = 10 \mu\text{m}$ and averaged. The standard deviations in G are smaller than the data points in Fig. 3(b).
- For the case of (iv) a small downstream gradient (left region of Fig. 2F in [16]), because the concentration values are so small, we use the same procedure as above, but for the raw concentration data

rather than the trial- and window-averaged data in Fig. 2F of [16], for better accuracy. The error bar on this point in Fig. 3(b) is the standard deviation across six experimental trials of the average G value in this region.

- For the above cases, cells migrated, on average, (i) up-gradient (Fig. 3C in [16], second box plot), (ii) up-gradient (Fig. 3C in [16], sixth box plot), (iii) nowhere (Fig. 3C in [16], fifth box plot; compare with control), and (iv) upstream (Fig. 3C in [16], seventh box plot). In the case of flow with no gradient, cells migrated upstream on average (Fig. 3C in [16], third box plot).

For Fig. 3(c):

- Typical cell surface concentrations of ephrin are on the order of $c_2 = 10^2 - 10^3 \mu\text{m}^{-2}$, and ephrin receptors have been measured to respond to these concentrations (see Fig. 3 in [31]). We use this range

[error bars in Fig. 3(c)].

- The diffusion constant of ephrin was measured at $D_2 = 2 \mu\text{m}^2/\text{s}$ (Fig. 2A in [31]).
- For head-to-head cell-cell collisions, the EGF concentrations used in [21] increase by $\Delta c = 3.3 \text{ nM}$ on top of backgrounds of $c = 4.1 \text{ nM}$, $c = 8.3 \text{ nM}$, and $c = 12.4 \text{ nM}$ (see Fig. 3c-e in [21]). Only $f = 40\%$ of this increase occurs within the cell microchannel, over a distance of approximately $d = 250 \mu\text{m}$, and the profile is linear within the microchannel (see Fig. S1e of [21]). Thus, $g = f\Delta c/d$. These three values of $G = g\sqrt{a^5/c}$ with $a = 10 \mu\text{m}$ are used in Fig. 3(c).
- The majority of cells migrated up-gradient (outcome 1 in Fig. 3a-e of [21]) when $c = 4.1 \text{ nM}$ and $c = 8.3 \text{ nM}$ (see right bars in Fig. 3c and d of [21]), whereas the majority of cells migrated away from the other cell (outcomes 2 and 3 in Fig. 3a-e of [21]) when $c = 12.4 \text{ nM}$ (see right bars in Fig. 3e of [21]).